



Design of a tunable resonant micromirror

Feng-Yu Lee^{a,1}, Xi Zhou^{b,1}, Xue'en Yang^b, Weileun Fang^{a,*}, Shih-Chi Chen^{b,c,**}

^a Department of Power Mechanical Engineering, National Tsing Hua University, Hsinchu, Taiwan, ROC

^b Department of Mechanical and Automation Engineering, The Chinese University of Hong Kong, Shatin, N.T., Hong Kong

^c Shenzhen Research Institute, The Chinese University of Hong Kong, Shenzhen 518057, People's Republic of China

ARTICLE INFO

Article history:

Received 22 December 2014

Received in revised form 17 August 2015

Accepted 17 August 2015

Available online 20 August 2015

Keywords:

Micromirror

Thermomechanical actuators

Tunable

Resonance

Electrostatic actuators

ABSTRACT

This paper presents the concept, theoretical analysis, microfabrication processes and experimental characterization of a micromirror with tunable resonant frequency. For scanning applications where a large scanning angle is required, comb-drive based micromirrors are typically operated at resonance due to the limited force/energy density of electrostatic actuators. However, errors in microfabrication processes often cause natural frequencies to offset from the design value. This issue may be resolved by a frequency-tunable micromirror. In our design, the shifting of the resonant frequency is achieved by adjusting the axial stress of the micromirror's torsion hinge via integrated chevron thermomechanical actuators. The scanning motion of the micromirror is generated by double silicon-on-insulator (SOI) wafer-based electrostatic comb-drive actuators. The experimental results show that the micromirror has achieved a frequency tuning range of approximately 3%, which is close to the analytic model. With precise frequency control, the micromirror may compensate the undesired frequency shift due to fabrication errors, which is useful for applications requiring precise scanning synchronization such as the laser scanning endomicroscope systems.

© 2015 Elsevier B.V. All rights reserved.

1. Introduction

The micromirror, or the microelectromechanical systems (MEMS) mirror, has a broad range of applications in miniaturized optics, fiber optics and endomicroscopy systems. Micromirrors exhibit high scanning speeds and large scan angles when driven at resonant frequencies. As reported in the literature, for example, an electrostatically actuated micromirror is capable of scanning at 32 kHz with a scan angle of 24.9° [1]. Due to the limited driving force of electrostatic actuators, e.g., comb-drives, and the high Q factors of silicon-based devices, micromirrors are often operated at their resonant frequencies to obtain sufficient scan angles; and their bandwidths are usually restricted to tens of hertz. For applications that require a precise operating frequency, e.g., video raster scanning, it is difficult to fabricate a micromirror with reliable performance due to the fabrication errors. Fabrication errors on the order of 100s of nanometer to a few microns can cause the resonant frequencies of a micromirror to deviate from their design

values by 100s to 1000s Hz. As such, shifting of the natural frequency of a micromirror has been a highly desired functionality for micro-scanners that generate their scanning motions based on resonance. Specifically, a tunable micromirror can be more precisely operated at a desired speed/frequency with proper control. This is particularly important while precise scanning frequency is required when synchronizing multiple scanning axis for 2-D or 3-D image acquisition, e.g., laser scanning two-photon endomicroscopy [2].

In this paper, we present the concept, design, and fabrication techniques for the tunable resonant micromirror that overcomes the limitations of existing systems. Fig. 1 shows the schematics of the prototype micromirror. The out-of-plane scanning actuation is achieved by dual layer vertical electrostatic comb-drive actuators [3,4] which are widely used in MEMS actuators due to the low power consumption and fast response. Chevron thermomechanical actuators (TMAs) [5,6] are integrated at both sides of the mirror to exert axial loads or stresses on the hinges to change the torsional stiffness based on stress-stiffening effect, thus enabling the micromirror to operate at a variable range of resonant frequencies. By supplying precisely predefined current on the TMAs, accurate resonant frequencies and mode shape controls can be achieved.

2. Actuation principles

The cross-section of the device is shown in Fig. 2(A). The micromirror is comprised of two active silicon layers, between

* Corresponding author.

** Corresponding author at: Shenzhen Research Institute, The Chinese University of Hong Kong, Shenzhen 518057, People's Republic of China.

E-mail addresses: fang@pme.nthu.edu.tw (W. Fang), scchen@mae.cuhk.edu.hk (S.-C. Chen).

¹ These authors contributed equally to this work.

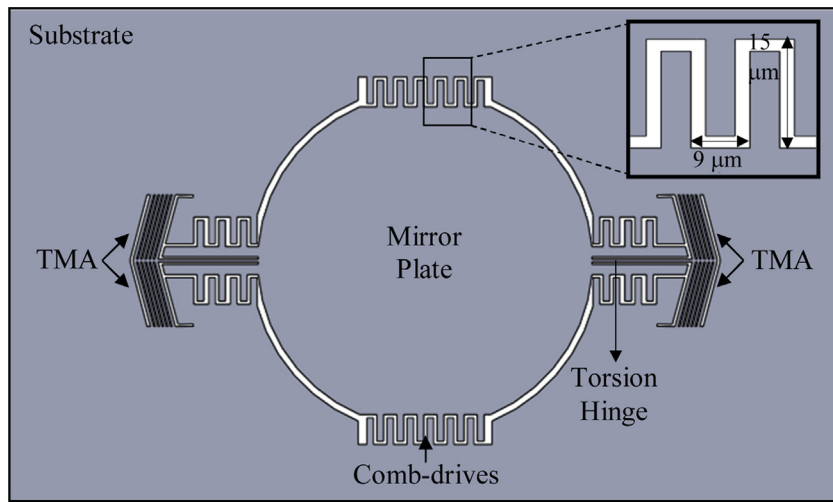


Fig. 1. Schematic of the tunable resonant micromirror; note that the size of the comb fingers is exaggerated.

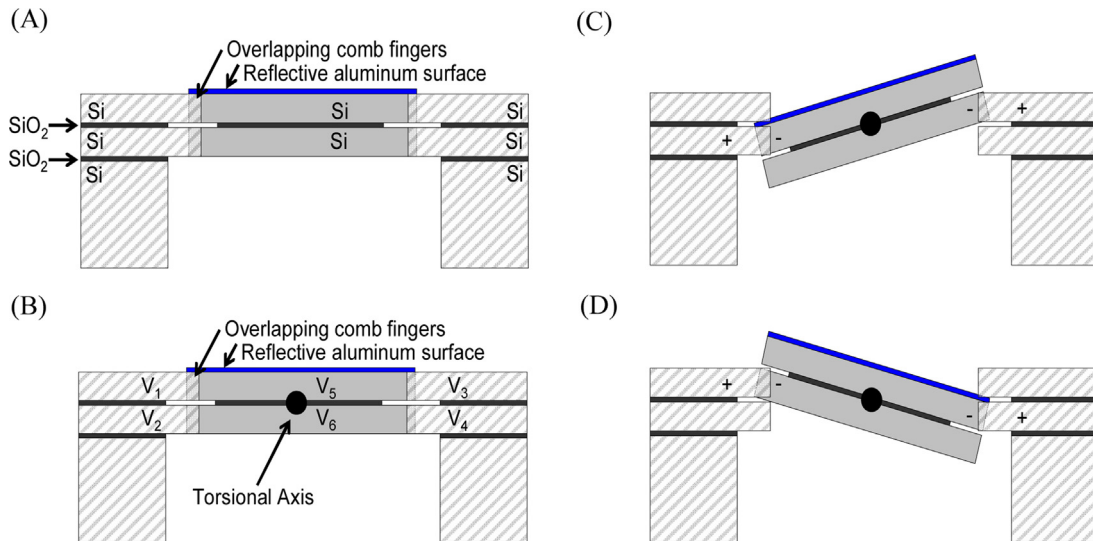


Fig. 2. Out-of-plane actuation mechanism: (A) cross-section of the composing layers of the micromirror; (B) cross-section of the micromirror with six individual electrodes; (C) and (D) alternation of electrode polarities for mirror scanning.

which is a layer of silicon dioxide that serves to insulate the two silicon layers both thermally and electrically. The two silicon layers have identical device geometries (mirror plate, TMAs and comb-drive fingers). The electrical access to the second silicon layer is achieved by removing the first silicon and silicon dioxide layer at specific locations on the device. With this structural design, we can achieve out-of-plane torsion motion by applying individual voltage level onto separate silicon layers, as shown in Fig. 2(B).

In order to generate the needed axial forces to induce stress-stiffening effect on the torsion hinge, two sets of chevron TMAs are connected to the torsion hinge (Fig. 1). When applying currents on the TMAs, the thermal expansion of these chevron beams will create axial loading on the torsion hinge. Detailed description of the actuating method is as follows:

2.1. In-plane actuation by TMAs

In-plane actuation refers to applying axial loads to the mirror hinges via two sets of chevron TMAs on both sides of the mirror. Note that as the device contains two structural (silicon) layers, actuating TMAs means energizing TMAs on both silicon layers.

TMA generate controlled mechanical motions via electrothermal transduction that provides relatively large force/displacement output, typically 1–4 orders of magnitude higher than electrostatic actuators or piezoelectric actuators [7]. Chevron TMAs consist of two slender beams that intersect at a shallow angle to provide motion amplification [5]. When a current passes through the beams, the resulting Joule heating causes the beams to strain in a way that enables actuation by force and/or displacement. TMAs are frequently used in high force, medium bandwidth, and high resolution applications [8,9] and herein suitable for the application.

2.2. Out-of-plane actuation by electrostatic comb-drive actuators

Out-of-plane actuation, as shown in Fig. 2(C) and (D), refers to applying vertical loads to the edge of the micromirror to generate angular scan motion. As illustrated in Fig. 2(B), the dual silicon layers and the released mirror structure create six electrodes for applying actuation voltages. The vertical comb-drive structure, as shown in Fig. 1, contains several hundreds of comb fingers that provide large sidewall overlapping area and close distance ($2\text{ }\mu\text{m}$) between electrodes. This configuration generates sufficient electrostatic actuation force, e.g., $10\text{s}-100\text{s }\mu\text{N}$, for scanning operation. The

Table 1

List of design parameters and material properties.

Symbol	Parameter	Value	Unit
c	Specific heat of silicon(298–800 K)	700–800	J/kg K
k_a	Thermal conductivity of air	0.03	W/mK
k_s	Thermal conductivity of silicon(298–800 K)	146–41	W/mK
r	Electrical resistivity of silicon	0.26	$\Omega \text{ cm}$
ρ	Density of silicon	2330	kg/m^3
E	Young's modulus of silicon	165	GPa
L_H	TMA beam length	400	μm
W_H	TMA beam width	20	μm
h	Structure thickness (total)	17	μm
g	Gap between TMA and substrate	500	μm
θ	Slanted angle	70	degree
W_T	Width of torsion bar	10	μm
N	Number of pairs of TMAs	6	N/A

operation procedure includes two steps: (1) positive voltages are applied to electrodes 2 and 3 while virtual ground (0 V) is applied to electrodes 5 and 6 to generate a torque to rotate the mirror in the counterclockwise direction, as shown in Fig. 2(C); (2) positive voltages are applied to electrodes 1 and 4 while virtual ground (0 V) is applied to electrodes 5 and 6 to generate a torque to rotate the mirror in the clockwise direction, as shown in Fig. 2(D). The actuation procedure is then repeated at the mirror's resonant frequency for continuous operation.

3. Modeling and design

In this section, we develop parametric models for the TMAs as well as the frequency tuning micromirror. The models are used to guide the design process and select design parameters to address requirements. Fig. 3 illustrates the parameters of a tunable resonant micromirror: D = the mirror's diameter, L_E = the length of comb-drive region, h = the thickness of mirror, W_T and L_H = the width and the length of the torsion hinge, W_H and L_H = the width and the length of thermal actuator beams, and θ = the angle between torsion hinge and thermal actuator beams.

3.1. Modeling of electrothermal actuation

This section presents parametric electrothermal modeling for the chevron TMA. Since chevron TMAs consist of slender beams of constant cross-section area, we can model the heat distribution in the TMA with a 1-D differential element as shown in Fig. 4. The differential element has a width of W_H , height of h and thickness of dx . When a current passes through the beam, the heat is transmitted by both thermal conduction and convection through the silicon and surrounding air respectively. The 1-D transient heat equation is presented in Eq. (1):

$$\begin{aligned} K_s \frac{dT(x, t)}{dx^2} + J^2 r - SF \times K_a \left(\frac{T(x, t) - T_\infty}{gh} \right) \\ - 2h_c (h + W_H) \left(\frac{T(x, t) - T_\infty}{W_H h} \right) = c\rho \frac{dT(x, t)}{dt} \end{aligned} \quad (1)$$

where K_s and K_a = thermal conductivity of silicon and air respectively. J = current density of the specified cross-section; g = gap between beams and substrate; h = beam height; r = electrical resistivity of silicon; h_c = convection coefficient; ρ = density of silicon; c = specific heat of silicon; SF = the shape factor, representing the ratio of conduction heat loss from the side and bottom of the beam to the heat loss from the boundaries of the beam only [10]. The values of each parameter used in the heat transfer analysis are listed in Table 1. Due to the small TMA size, which leads to a small Biot number, and the relatively large gaps between the TMAs and the substrate, heat conduction and convection

through the surrounding air can be neglected [11]. More specifically, heat dissipation due to silicon conduction ($K_s (dT(x, t) dx^2)$) at 800 K is calculated to be $4.1 \times 10^{13} \text{ W/m}^3$, which is four orders of magnitude larger than the effects of air convection ($2h_c (h + W_H) (T(x, t) - T_\infty) / W_H h = 4.1 \times 10^9 \text{ W/m}^3$) and air conduction ($SF \times K_a (T(x, t) - T_\infty) / gh = 3.48 \times 10^9 \text{ W/m}^3$). Accordingly, the transient heat equation can be reduced to:

$$K_s \frac{dT(x, t)}{dx^2} + J^2 r = c\rho \frac{dT(x, t)}{dt} \quad (2)$$

The corresponding boundary conditions are

$$T(0, t) = T(2L_H, t) = T(x, 0) = T_{\text{room}} \quad (3)$$

where T_{room} is the room temperature, assumed to be a constant. If we only consider the steady-state solution of Eq. (2), the solution can be expressed as

$$T(x) = -\frac{J^2 r}{2K_s} x^2 + \frac{J^2 r}{K_s} L_H x + T_{\text{room}} \quad (4)$$

Thus, the total thermal expansion of the TMA beam is

$$\Delta L = \int_0^{L_H} \alpha [T(x) - T_{\text{room}}] dx \quad (5)$$

where α is the coefficient of thermal expansion of silicon. Since the axial stiffness of the torsion bar is much greater than the bending stiffness of the TMAs, the resulting axial force on the torsion bar exerted by the TMAs can be approximated as

$$F_{\text{TMA}} \approx 2N \frac{\Delta L}{L_H} W_H h E \times \cos\theta \quad (6)$$

where E = the Young's modulus of silicon; N = the number of pairs of TMAs connected to the torsion bar. From Eqs. (4)–(6), the resulting axial stress, S , can be expressed as a function of the input current, I , in Eq. (7).

$$S = \frac{2}{3} I^2 r \frac{\alpha E}{NK_s} \frac{L_H^2}{W_H W_T h^2} \cos\theta \quad (7)$$

Note that in Eq. (1) the material properties, including r , α , E and K_s , are assumed to be constant. However, when the TMAs are operated over a wide temperature range, the temperature-dependent properties can lead to non-linear phenomena and inaccurate modeling results. To address this issue, we developed a nonlinear model based on finite difference method (FDM). Since our devices were made with antimony-doped wafers and temperature dependent properties of such wafers have not been reported in the literature, we use material properties of phosphorus-doped wafers [9] to construct our nonlinear model as they reside in the same column of the periodic table. Accordingly, Eq. (2) is approximated by the following expression:

$$\begin{aligned} T^*(x, t + \Delta t) = \alpha^* \times T^*(x - \Delta x, t) + (1 - 2\alpha^*) \times T^*(x, t) + \alpha^* \\ \times T^*(x + \Delta x, t) + \beta^* \end{aligned} \quad (8)$$

where Δx = increment of length; Δt = increment of time; α^* and β^* are temperature-dependent factors that can be expressed as:

$$\alpha^* = \frac{K_s}{c\rho} [T^*(x, t)] \times \frac{\Delta t}{\Delta x^2} \quad (9)$$

$$\beta^* = \frac{J^2 r}{c\rho} [T^*(x, t)] \times \Delta t \quad (10)$$

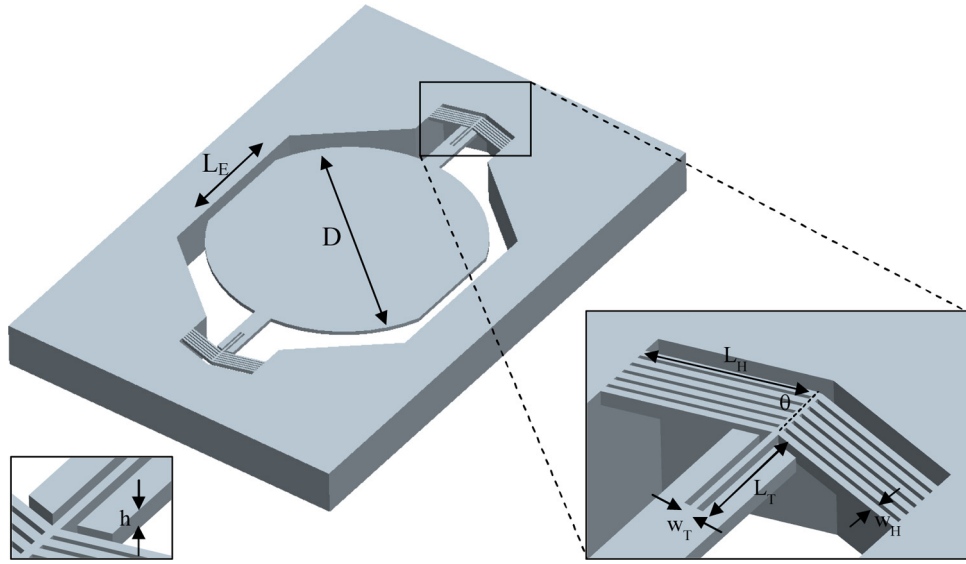


Fig. 3. CAD model and design parameters of the tunable micromirror.

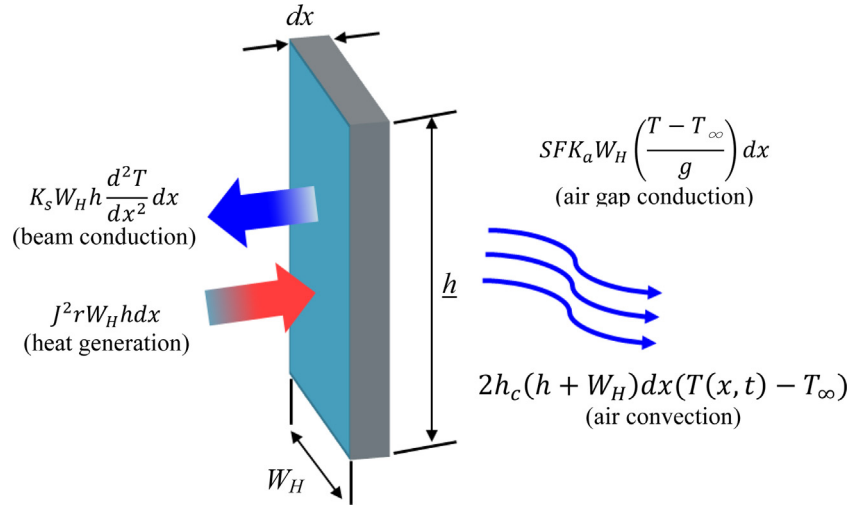


Fig. 4. The schematic plot of the heat flow at a specified cross-section.

If $0 < \alpha^* \leq 0.5$, the approximated $T^*(x, t)$ will converge to the solution $T(x, t)$. The resulting deformation ΔL^* and axial stress S^* are

$$\Delta L^* = \sum_{n=1}^{L_H/\Delta x} \alpha [T^*(x, t)] \times [T^*(x, t) - T_{\text{room}}] \quad (11)$$

$$S^* = 2N \frac{\Delta L^*}{L_H} \frac{W_H}{W_T} E \times \cos\theta \quad (12)$$

3.2. Modeling of stiffness tuning

When the temperature of the TMAs rises, the pull-force-induced axial stress will “stretch” the torsion hinge to generate a stress-stiffening effect, which increases the torsion stiffness, and furthermore, the torsion resonance. Given a torsion hinge with a rectangular section ($h > W_T$), its torsion stiffness K_T , when subjected to axial stress S , can be expressed by Eq. (13) [12,13]:

$$K_T = \frac{\kappa G}{L_T} \left[1 + \frac{1}{4} \left(\frac{h}{W_T} \right)^2 \frac{S}{G} \right] \quad (13)$$

where,

$$\kappa = h w_T^3 \left[\frac{1}{3} - 0.21 \frac{w_T}{h} \left(1 - \frac{w_T^4}{12h^4} \right) \right] \quad (14)$$

From Eqs. (7) and (13), we can find the functional relationship between the torsion stiffness and input current as:

$$\Delta K_T \propto I^2 r \frac{\alpha E}{NGK_s} \frac{L_H^2}{W_H W_T^3} \cos\theta \quad (15)$$

Accordingly, Eq. (15) can be used to guide the design process for achieving specific frequency tuning range. Devices with higher ΔK_T values will have a larger tuning range.

In our design, we aim to achieve a 3–5% frequency tuning range with minimized (1) internal stresses and (2) operating power. First, we consider the stress concentration effect and fabrication limit. The maximum shear stress for a rectangular cross-section torsion hinge can be calculated as [14]

$$\tau_{\max} = \frac{3T}{hw_T^2} \left[1 + 0.6095 \left(\frac{w_T}{h} \right) + 0.8865 \left(\frac{w_T}{h} \right)^2 - 1.8023 \left(\frac{w_T}{h} \right)^3 + 0.9100 \left(\frac{w_T}{h} \right)^4 \right] \\ \cong \frac{3T}{h} \left[\frac{1}{W_T^2} + 0.6095 \left(\frac{1}{hW_T} \right) + 0.8865 \left(\frac{1}{h^2} \right) + \dots \right] \text{ for } h \geq w_T \quad (16)$$

where T = the applied torque; h and W_T = the thickness and width of the torsion hinge respectively. The generalized von Mises stress in the torsion hinge can be expressed as:

$$\sigma_v = \sqrt{\frac{(\sigma_{11} - \sigma_{22})^2 + (\sigma_{22} - \sigma_{33})^2 + (\sigma_{33} - \sigma_{11})^2 + 6(\sigma_{12}^2 + \sigma_{23}^2 + \sigma_{31}^2)}{2}} \approx \sqrt{S^2 + 3\tau_{\max}^2} \quad (17)$$

where we find $S \propto 1/W_T h^2$ and $\tau_{\max} \propto 1/h W_T^2$ from Eqs. (7) and (16).

Observing Eqs. (7) and (17), we learn high-tuning range and low stress concentration can be achieved with high aspect ratio beam cross-sections, i.e., h/W_T , where W_T is limited by the fabrication process to $\sim 5 \mu\text{m}$. As a result, in our first generation design, aspect ratios of 1–3 were selected under conservative fabrication considerations. (The mirror is fabricated with a double SOI wafer, where $h = 17 \mu\text{m}$, discussed in Section 4.) Driving power can be optimized to generate sufficient axial force by fine-tuning the TMA angles (θ) with an appropriate number of TMAs (N). The axial stiffness of the TMA train is proportional to the number of TMAs; however, increasing the number of TMAs also increases the driving power. Optimal power efficiency is achieved when the axial stiffness of the TMA train is equal to that of the torsion hinge via considering mechanical impedance matching [2]. Following this design strategy, we designed our TMA train with $N = 6$ and $\theta = 20^\circ$.

3.3. Operating modes of micromirror

In order to obtain the desired operating modes of a micromirror within the designated device envelope, the resonance should be determined by specific design parameters. For the out-of-plane torsion mode, the resonance is calculated as:

$$\omega_{\text{Torsion}} = \sqrt{\frac{K_T}{J_T}} \quad (18)$$

where K_T = the torsional stiffness as described above, and J_T = the moment of inertia of the scanning mirror which can be expressed in this equation:

$$J_T = \frac{\rho h D^4}{64} \left(\pi - 2\alpha + \frac{\sin 4\alpha}{2} \right) \quad (19)$$

where

$$\alpha = \sin^{-1} \left(\frac{L_E}{D} \right) \quad (20)$$

Also, for the out-of-plane piston mode, the resonance is calculated as:

$$\omega_{\text{piston}} = \sqrt{\frac{K_B}{M}} \quad (21)$$

where K_B = bending stiffness of the torsion hinge, and M = total mass of the mirror. K_B and M can be expressed as follows:

$$K_B = 2 \frac{E w_T h^3}{L_T^3} \quad (22)$$

$$M = \frac{D^2 \rho h}{4} (\pi - 2\alpha + \sin 2\alpha) \quad (23)$$

For scanning application, it is important to separate the torsion mode from the piston mode to improve scanning stability. Note that in the first order analysis above, the stiffness of the TMA is not taken into account as its torsion and out-of-plane bending stiffness is much higher than the torsion hinge.

3.4. Estimation of quality factor

For the torsional motion of the micromirror, the quality factor can be approximated as

$$Q \approx \frac{\sqrt{J_T K_T}}{C_q} \quad (24)$$

where the J_T is the moment of the inertia of the scanning mirror, K_T is the torsional stiffness, and C_q is the coefficient of the damping torque, which is derived from the mirror plate and the comb-fingers.

$$C_q = C_{\text{mirror}} + C_{\text{comb}} \quad (25)$$

The damping coefficient of the mirror plate and the comb-drive fingers can be calculated from [15,16]

$$C_{\text{mirror}} = \frac{192 \mu D (D^2 - L_E^2)^{\frac{5}{2}}}{\pi^6 g^3} \times \sum_{n=1,2,\dots} \sum_{m=1,2,\dots} \frac{1}{(2n)^4 (2m-1)^2} \\ \approx 15.3 \frac{\mu D (D^2 - L_E^2)^{\frac{5}{2}}}{\pi^6 g^3} \quad (26)$$

$$C_{\text{comb}} = \frac{N_{\text{finger}} D^2}{4} \frac{L_{\text{finger}} h}{g_{\text{finger}}} \frac{\mu}{1 + 2K_n + 0.2K_n^{0.788} e^{-K_n/10}} \quad (27)$$

where N_{finger} is the number of the comb-fingers, L_{finger} is the length of the finger, and the g_{finger} is the gap between fingers. The Knudsen number, K_n , is a function of the gas mean free path λ and the finger gap.

$$K_n = \frac{\lambda}{g_{\text{finger}}} \quad (28)$$

4. Fabrication process and results

4.1. Fabrication process

The fabrication process of the tunable resonant micromirror is as illustrated in Fig. 5 [17].

Step 1: A 200 mm diameter double SOI wafer that consisted of five layers: from top to bottom were 1st silicon device layer (8 μm), silicon dioxide (1 μm), 2nd silicon device layer (8 μm), silicon dioxide (1 μm) and silicon handling layer (500 μm).

Step 2: The features that support the actuator's electrical contacts were created via deep reactive ion etching (DRIE) on the 1st silicon device layer; the oxide layer under the 1st device layer was removed by buffered oxide etching (BOE).

Step 3: Aluminum electrical contact pads were patterned selectively on the features created in Step 2.

Step 4: The micromirror geometry was etched through the 1st device layer to the 2nd device layer.

Step 5: After applying resist-coating, the wafer was mounted onto a handling/supporting wafer.

Step 6: A through-etch using DRIE on the back-side of the wafer was performed to release the micromirror, where the oxide layer served as an etch stop.

Step 7: The supporting wafer was removed from the 1st device layer.

Step 8: A BOE was performed to release the structure.

4.2. Fabrication results

The fabrication and packaging result of a micromirror are shown in Fig. 6, where the diameter of this particular micromirror is 2.5 mm. The torsion hinge is 300 μm in length and connected to a set of outward-pointing TMAs. The TMAs on either side of the mirror consist of six parallel chevron beams that intersect the torsion

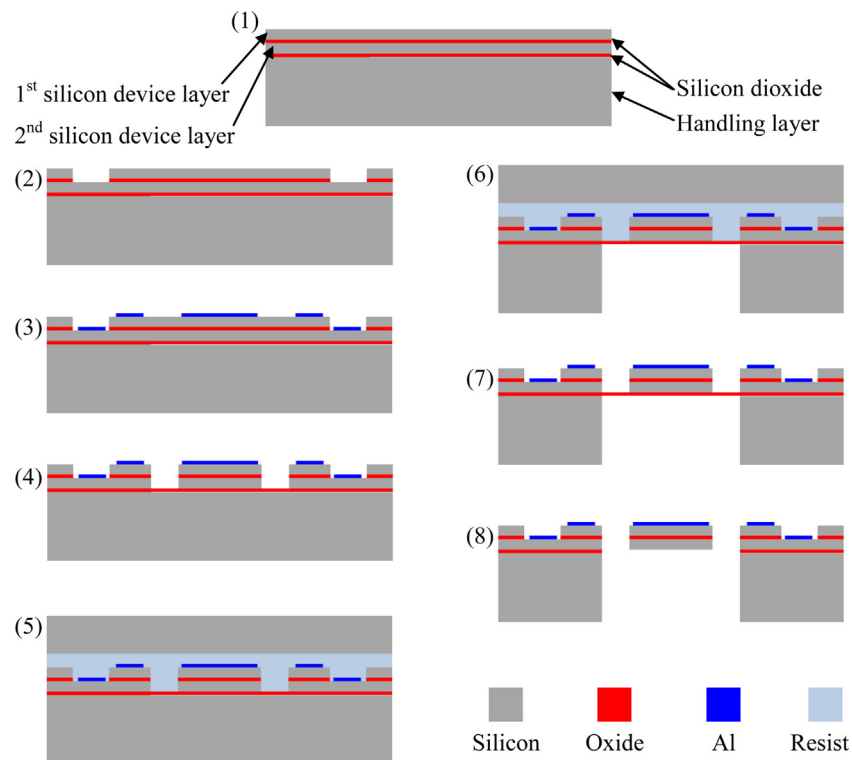


Fig. 5. Fabrication process of the tunable resonant micromirror.

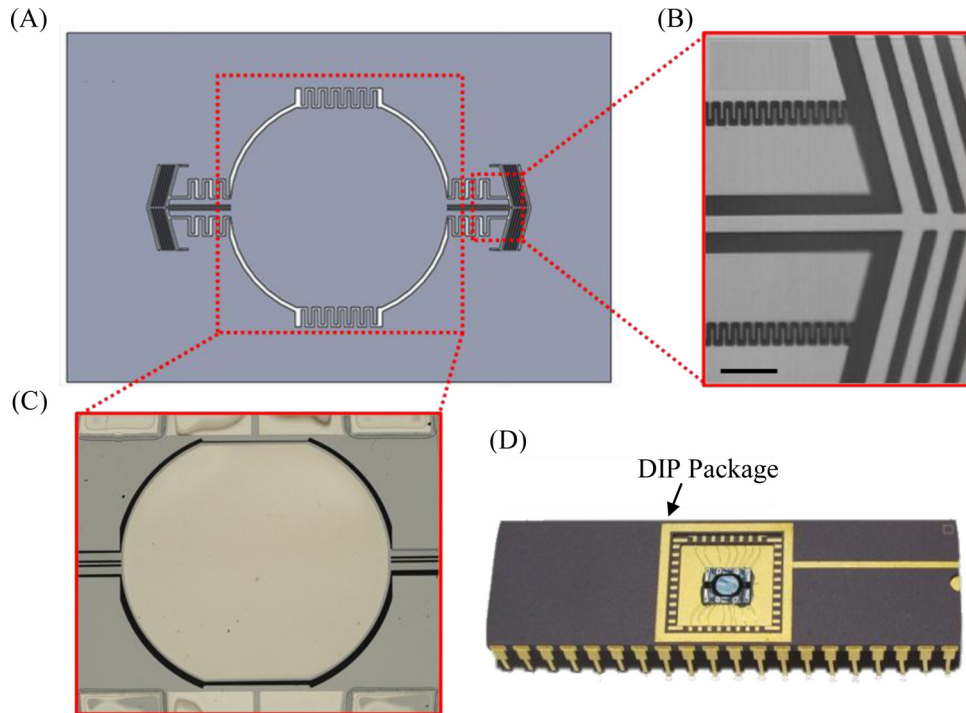


Fig. 6. Images of the fabricated micromirror with DIP package: (A) schematics of the micromirror; (B) microfabricated comb-drive actuators; the scale bar is 60 μm ; (C) top view of the aluminum coated mirror surface; the diameter of the micromirror is 3 mm; (D) micromirror packaged with a 40-pin DIP chip.

hinge to increase the axial force output. Electrostatic comb-drive actuators are integrated into the device to drive the micromirror, as shown in Fig. 6(B). For testing purpose, the fabricated micromirror was attached to a 40-pin ceramic DIP using an anaerobic adhesive glue and then wired-bonded to DIP pads, as shown in Fig. 6(D).

The surface profile of the micromirror was first measured by a white light interferometer (Wyko NT1100) at room temperature, where the radius of curvature of the mirror plate was 100.23 mm, and the roughness was 68.7 nm RMS due to the BOE process. Further characterization shows the radius of curvature slightly

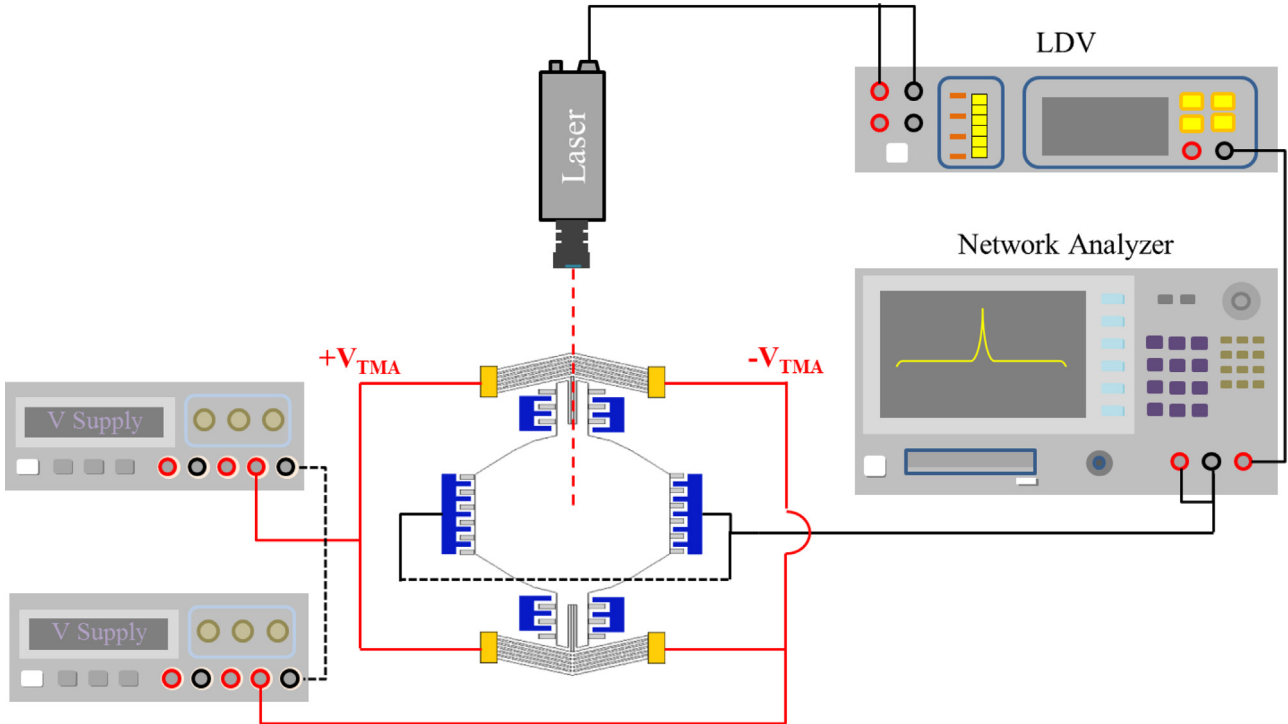


Fig. 7. Experimental set-up for extracting resonant frequencies.

increases with increasing temperature at a rate of 0.125%/K, i.e., the mirror plate becomes flatter at high temperature. As the mirror plate is not flat due to the tensile stress in the reflective layer (Al), the radius of curvature can be improved by either increasing the device layer thickness or decreasing the reflective layer thickness.

5. Experimental setup and results

5.1. Measurement set-up

The schematic of the experimental set-up is shown in Fig. 7. In order to extract the resonant frequency, we used a network analyzer to generate electrical signals for the electrostatic comb-drives

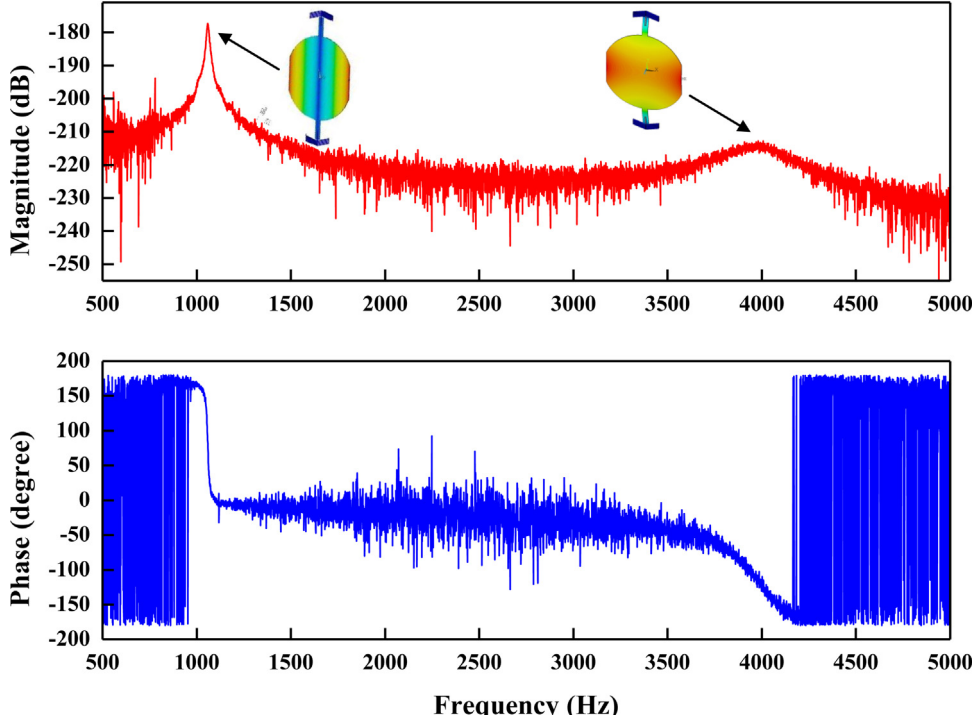


Fig. 8. Frequency response and mode shapes of the micromirror with no driving currents on TMAs.

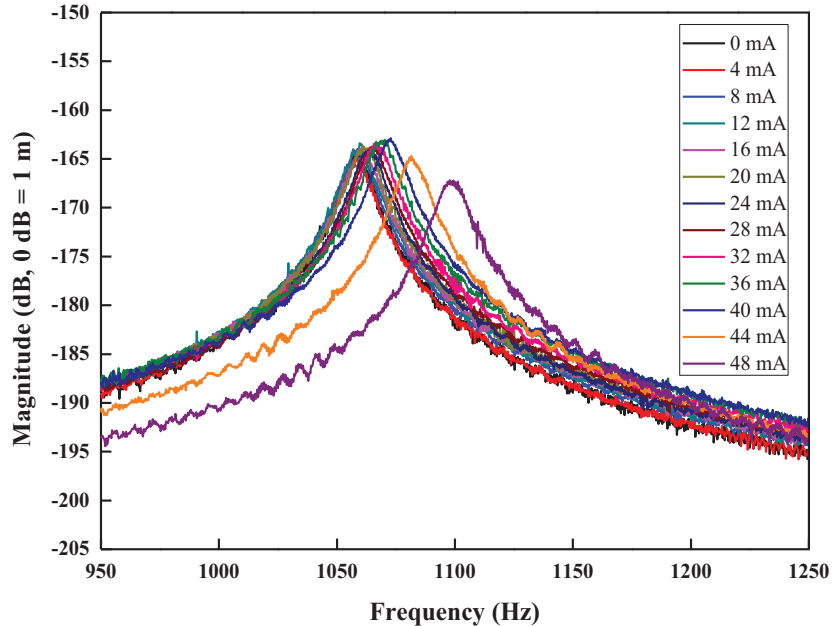


Fig. 9. Frequency response of the micromirror with respect to different applied currents.

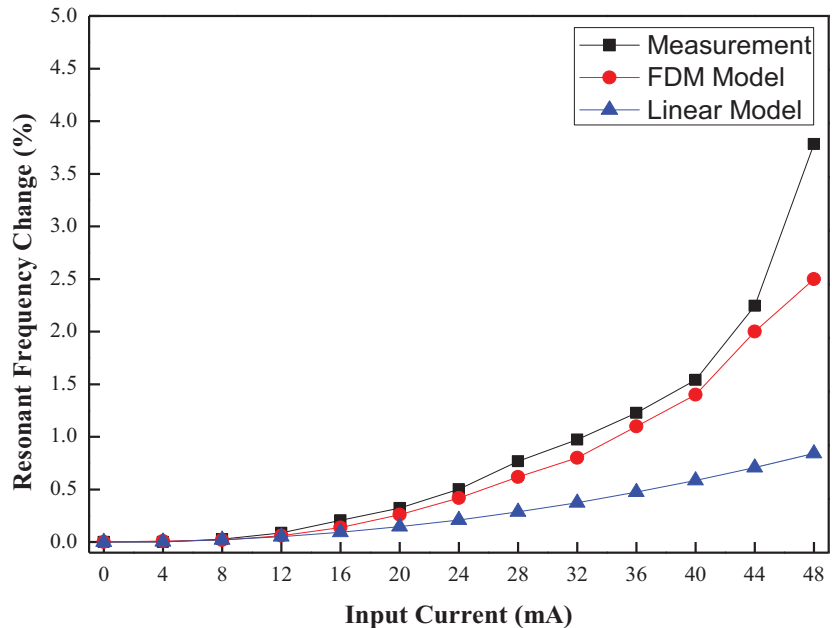


Fig. 10. Relationship between the torsional resonance change and the applied current.

and a laser doppler vibrometer (LDV) to analyze the velocity and the displacement signals, where the bias voltage of the comb-drive actuator was precisely controlled to maintain a stable driving force. This was achieved by using two voltage sources to generate a voltage difference on the TMAs (as shown in Fig. 7, $+V_{TMA}$ and $-V_{TMA}$). The input current can be controlled by adjusting the voltage difference, while the electrical potential on the mirror plate was kept constant during the operation. We expect the resonant frequency of the micromirror to increase with increasing voltage difference (current).

5.2. Result and discussion

The frequency response of the fabricated micromirror was investigated. In order to distinguish the difference from one mode to another, comb-drive actuators on only one side of the

micromirror were employed to induce an unbalanced force on the micromirror. By doing so we were able to identify different modes in a single sweep measurement. As shown in Fig. 8, the frequency response of the micromirror ranges from 500 Hz to 5 kHz. The measurement result showed 2 resonance peaks in this sweeping range accompanied by a corresponding -180° phase change. The first resonance peak at 1060 Hz was the torsion mode, i.e., the chief goal of the design. The second resonance peak was the out-of-plane piston mode. The quality factor of the torsion mode is ~ 130 , which is smaller than our estimation ($Q \approx 368$, from Eq. (24)). This may be due to additional damping effect, including higher ambient pressure and the geometry discrepancy.

Once the operating mode was confirmed, we used all of the comb-drive actuators to drive the micromirror, ensuring it will be operated in the torsion mode. At the same time, we varied the applied current on the TMAs and measured the frequency response

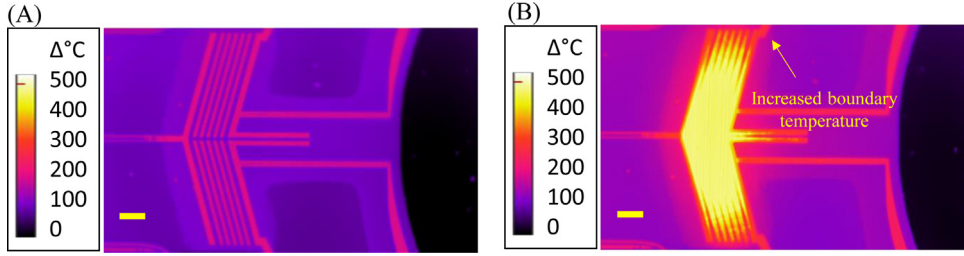


Fig. 11. Infrared images under different TMA input currents: (A) 10 mA; (B) 50 mA. The scale bar in the image is 100 μm .

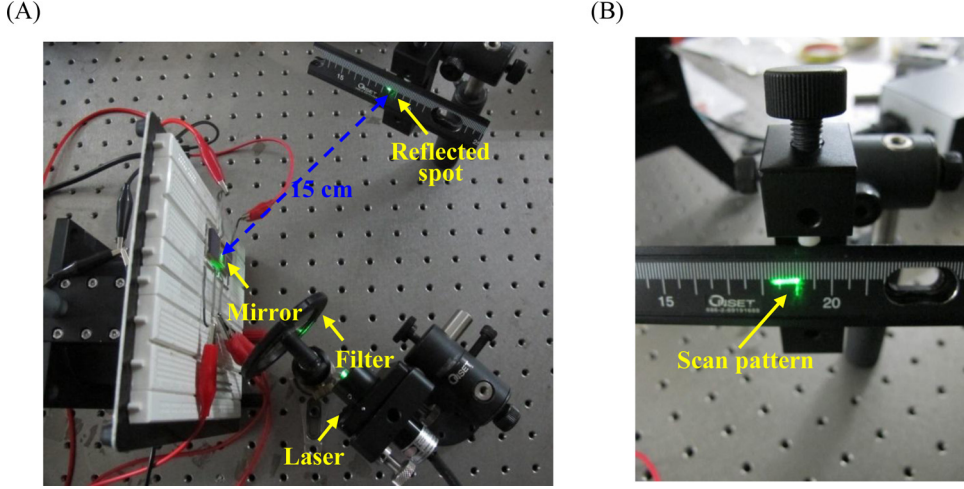


Fig. 12. Scan pattern measurement: (A) measurement setup, (B) scan pattern (5 V AC, 30 V V_{bias}).

around the torsional resonance. The results are shown in Fig. 9, validating the increase of resonant frequency of the micromirror in response to the rise of applied current on TMAs. Such result corroborated our design concept: due to the thermal expansion of the chevron beams, the TMAs will stretch the torsion hinge to generate axial stress. The stress will then increase the torsional stiffness (stress-stiffening effect) and eventually, the torsional resonance as a result. The measured relationship between the torsional resonance and the applied current is shown in Fig. 10 with modeling results.

Fig. 10 demonstrates a non-linear characteristic of the frequency tuning effect with respect to the applied current. When the applied current first increases, the resonant frequency increases slightly. The resonant frequency increases more effectively when the applied current continues to increase. Such non-linear characteristic is due to Joule heating as well as temperature dependent thermal properties of silicon, e.g., thermal conductivity and electrical resistivity. For Joule heating, the heat generated on a resistor, i.e., the chevron TMAs, is proportional to the square of the applied current; this effect is captured by both the linear and FDM model when the applied current is below 12 mA. At higher current (or temperature), the frequency shift becomes more effective due to the temperature dependent thermal properties. This tendency is predicted by our FDM models in Eqs. (7)–(13) when the current is below 44 mA. When the input current is greater than 44 mA, the FDM model fails to predict the further increased frequency shift. To investigate the issue, we took infrared images of the TMAs during operation at 10 mA and 50 mA, respectively. The results are presented in Fig. 11(A) and (B) respectively. Analyzing the images, we found at 50 mA the temperature is elevated both at the boundaries of the TMAs and at part of the torsion hinge, particularly the part connected to the TMAs. The combined effects of the increased temperature on the boundaries and the torsion hinge cause the TMA to generate more axial stresses, which explain the FDM model

under-estimates the tuning range when input currents are above 44 mA.

To achieve more efficient frequency-tuning in our next-generation device, we will modify the TMAs design by utilizing the “stress-softening” effect. In other words, the chevron TMAs will point inward and the torsional resonance will decrease due to compressive stresses when the applied current rises. Since the temperature coefficient of elasticity (TCE) of silicon has a negative value (-60 ppm/K) [18], the stress-softening effect will be further enhanced with the increasing temperature of the torsion hinge. Note that buckling may be an issue in this configuration, but it can be avoided with proper design.

Lastly, we devised a line-scanning experiment to measure the scan angle of the micromirror. The experimental setup and the line scan pattern are shown in Fig. 12(A) and (B) respectively. The results indicate that the micromirror generates a 3.8° optical scanning angle when driven by a 5 V AC signal and 30 V bias voltage. Although scan angle is relatively small due to a thin device layer ($17 \mu\text{m}$) and a large mirror diameter (2.5 mm), it satisfies many laser scanning applications, e.g., confocal or multiphoton laser scanning microscopes, where a large mirror plate and precise operating frequency is critical.

6. Conclusion

This paper presents the concept, theoretical analysis, micro-fabrication processes and experimental characterization of the micromirror with tunable resonant frequency. The shifting of the resonant frequency is achieved by adjusting the axial stress on the micromirror's torsion hinge via the integration of chevron TMAs which exploits the stress-stiffening effect to increase torsional resonance. Our first-generation device achieved a frequency tuning range of approximately 3%, which matches well with our parametric model and provides sufficient tuning range to overcome fabrication errors for precise frequency control. Next generation

micromirrors will be designed for a larger frequency-tuning range using the “stress-softening” effect.

Acknowledgements

This work is supported by the HKSAR Research Grants Council (RGC) General Research Fund (GRF/ECS), CUHK 439813: a High-Resolution Nonlinear Optical Endomicroscope Based on Tunable Micromirror, the National Natural Science Foundation of China (NSFC), General Program, #51375415: Development of a Flexure-based Optical Scanning System and a Multimodal Non-linear Endomicroscope for *in vivo* Biological Studies, and the CUHK Start-up Funding for Collaboration with Strategic Partners in Taiwan: Development of Multiple Degrees of Freedom High-speed Scanning Technologies for Endomicroscopy Applications.

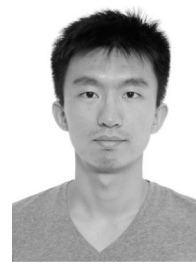
References

- [1] R.A. Conant, J.T. Nee, K.Y. Lau, R.S. Muller, *A Flat High-Frequency Scanning Micromirror*, Hilton Haed Solid-State Sensor and Actuator Workshop, 2000, 2015, pp. 6–9.
- [2] S.-C. Chen, H. Choi, T.C. So, M.L. Culpepper, Thermomechanical actuator-based three-axis optical scanner for high-speed two-photon endomicroscope imaging, *J. Microelectromech. Syst.* 23 (2013) 570–578.
- [3] U. Krishnamoorthy, D. Lee, O. Solgaard, Self-aligned vertical electrostatic combdrives for micromirror actuation, *J. Microelectromech. Syst.* 12 (2003) 458–464.
- [4] S. Kwon, V. Milanovic, L.P. Lee, Large-displacement vertical microlens scanner with low driving voltage, *Photonics Technol. Lett.* 14 (2002) 1572–1574.
- [5] L. Que, J.-S. Park, Y.B. Gianchandani, Bent-Beam Electro-Thermal Actuators for High Force Applications, *Micro Electro Mechanical Systems*, Orlando, FL, USA, 1999, pp. 31–36, January.
- [6] S.-C. Chen, M.L. Culpepper, Design of contoured microscale thermomechanical actuators, *J. Microelectromech. Syst.* 15 (2006) 1226–1234.
- [7] D.J. Bell, T.J. Lu, N.A. Fleck, S.M. Spearing, MEMS actuators and sensors: observations on their performance and selection for purpose, *J. Micromech. Microeng.* 15 (2005) S153–S164.
- [8] N.B. Hubbard, L.L. Howell, Design and characterization of a dual-stage, thermally actuated nanopositioner, *J. Micromech. Microeng.* 15 (2005) 1482–1493.
- [9] S.-C. Chen, M.L. Culpepper, Design of a six-axis micro-scale nanopositioner—μHexFlex, *Precis. Eng.* 30 (2006) 314–324.
- [10] R. Hickey, D. Sameoto, T. Hubbard, M. Kujath, Time and frequency response of two-arm micromachined thermal actuators, *J. Micromech. Microeng.* 13 (2003) 40–46.
- [11] J.M. Maloney, D.S. Schreiber, D.L. Devoe, Large-force electrothermal linear micromotors, *J. Micromech. Microeng.* 14 (2004) 226–234.
- [12] Y. Zhu, A. Corigliano, H.D. Espinosa, A thermal actuator for nanoscale *in situ* microscopy testing: design and characterization, *J. Micromech. Microeng.* 16 (2006) 242–253.
- [13] M.A. Biot, Increase of torsional stiffness of a prismatical bar due to axial tension, *J. Appl. Phys.* 10 (1939) 860–864.
- [14] W.C. Young, R.G. Budynas, *Roark's Formulas for Stress And Strain*, McGraw-Hill, New York, NY, 2002.
- [15] A. Minikes, I. Bucher, G. Avivi, Damping of a micro-resonator torsion mirror in rarefied gas ambient, *J. Micromech. Microeng.* 15 (2005) 1762–1769.
- [16] T. Veijola, M. Turowski, Compact damping models for laterally moving microstructures with gas-rarefaction effects, *J. Microelectromech. Syst.* 10 (2001) 263–273.
- [17] S.-C. Chen, M.L. Culpepper, Multiple degree of freedom micro electro-mechanical system positioner and actuator, U.S. Patent, 7451596, (2008).
- [18] R. Melamud, S.A. Chandorkar, B. Kim, H.-K. Lee, J.C. Salvia, G. Bahl, M.A. Hopcroft, T.W. Kenny, Temperature-insensitive composite micromechanical resonators, *J. Microelectromech. Syst.* 18 (2009) 1409–1419.

Biographies



Feng-Yu Lee was born in Pingtung, Taiwan, in 1987. He received the B.S. and M.S. degree in Power Mechanical Engineering from the National Tsing Hua University, Taiwan, in 2007 and 2009, respectively. He is currently a Ph.D. candidate in the Department of Power Mechanical Engineering, National Tsing Hua University. His M.S. work includes the development of a dual-axis micro positioning stage, which utilizes the Lorentz force actuation. His present research is focused on the microscale vibratory gyroscope, including the decoupled mechanism



design, multi-axis integration and microfabrication process development.

Xi Zhou received his B.S. degree in Thermal Science and Energy Engineering from the University of Science and Technology of China in 2007. He is currently a Ph.D. candidate in the Department of Mechanical and Automation Engineering at the Chinese University of Hong Kong. Since January 2015, he has been a visiting student in the Department of Mechanical Engineering at the Massachusetts Institute of Technology. His current research interests include precision machine design, microscale system design and fabrication. Xi Zhou is a student member of the American Society for Precision Engineering (ASPE).



Xue'en Yang was born in Guangdong, China, in 1975. She received the B.S. degree in mechanical engineering from the University of California, Berkeley, in 1999. She received the S.M. and Ph.D. degrees in mechanical engineering from the Massachusetts Institute of Technology (MIT), Cambridge, in 2001 and 2005, respectively. Dr. Yang is currently a visiting scholar in the Department of Mechanical and Automation Engineering at the Chinese University of Hong Kong (CUHK). She is interested in the design, simulation, and fabrication of MEMS devices with emphasis in Power MEMS and RF MEMS, and in particular, their applications by means of system design and integration.



Weileun Fang (M'06–SM'11) was born in Taipei, Taiwan. He received the Ph.D. degree from Carnegie Mellon University, Pittsburgh, PA, in 1995. His doctoral research focused on the determination of the mechanical properties of thin films using micromachined structures. In 1995, he was a Postdoctoral Researcher with the National Synchrotron Radiation Research Center, Taiwan. Since 1996, he has been with the Department of Power Mechanical Engineering, National Tsing Hua University, Hsinchu, Taiwan, where he is currently a Professor as well as a Faculty Member of the Institute of NanoEngineering and MicroSystems. In 1999, he was with Prof. Y.-C. Tai at the California Institute of Technology, Pasadena, CA, as a Visiting Associate. His research interests include MEMS with emphasis on microfabrication/packaging technologies, CMOS MEMS, CNT MEMS, microoptical systems, microsensors and actuators, and characterization of thin-film mechanical properties. Dr. Fang is currently an Editorial Board Member of the Journal of Micromechanics and Microengineering and the IEEE TRANSACTIONS ON DEVICE AND MATERIALS RELIABILITY and an Associate Editor of the IEEE SENSORS JOURNAL and Journal of Micro/Nanolithography, MEMS, and MOEMS. He has served as the chief delegate of Taiwan to the World Micromachine Summit since 2008 and the General Chair of the World Micromachine Summit 2012. He also served on the Technical Program Committee (TPC) of IEEE MEMS 2004, MEMS 2007, and MEMS 2010, the regional TPC of Transducers 2007, and the Executive Program Committee of Transducers 2009–2013. He has been a member of the International Steering Committee of Transducers since 2009. Moreover, he also serves as a Technical Consultant for many MEMS companies in Taiwan.



Shih-Chi Chen received his B.S. degree in Mechanical Engineering from the National Tsing Hua University, Taiwan, in 1999. He received his S.M. and Ph.D. degrees in Mechanical Engineering from the Massachusetts Institute of Technology, Cambridge, in 2003 and 2007, respectively. Following his graduate work, he entered a post-doctoral fellowship in the Wellman Center for Photomedicine, Harvard Medical School, where his research focused on biomedical optics and endomicroscopy. He is currently an Assistant Professor in the Department of Mechanical and Automation Engineering at the Chinese University of Hong Kong (CUHK). Before joining CUHK, he was a Senior Scientist at Nano Terra, Inc., a start-up company founded by Prof. George Whitesides at Harvard University, to develop novel methods and instruments for the control of various interface functionalities. His current research interests include precision engineering, biomedical devices/optics, MEMS, and nanomanufacturing. Prof. Chen is a Member of the American Society of Mechanical Engineers (ASME) and the American Society for Precision Engineering (ASPE). He is the recipient of a 2003 R&D 100 Award for the design of a microscale six-axis nanopositioner.